Elliptic flow of π, K, p and ϕ in Pb-Pb collisions at the Large Hadron Collider

Bachelor thesis
by
Maria Mårtenson

Supervised by
David Silvermyr

LUND
UNIVERSITY

Division of Particle Physics
December 2015

Abstract

Data extracted from Pb-Pb collisions at $\sqrt{s_{NN}} = 2.76$ TeV measured with the ALICE detector is used for analyzing the azimuthal anisotropic expansion in momentum space at different collision centralities for identified particles. The results are obtained with the event-plane method and an invariant mass analysis. The elliptic flow parameter, v_2, is presented as a function of transverse momentum p_T for $\pi^{\pm}$, $K^{\pm}$, p+$\overline{p}$ and ϕ, up to $p_T = 3.6$ GeV/c and for different event centrality selections. Further, the obtained measurements of v_2 values for $\pi^{\pm}$, $K^{\pm}$ and p+$\overline{p}$, are scaled with the number of constituent quarks n_q and presented as a function of the transverse kinetic energy EK_T/n_q.

Populärvetenskaplig sammanfattning

Partikelfysik är det område inom den vetenskapliga disciplinen fysik som studerar materiens minsta byggstenar och hur de växelverkar mellan varandra. De partiklar som bygger upp all observerad materia kallas kvarkar och leptoner. Dessa partiklar växelverkar med varandra genom gluoner, som binder ihop och överför diskreta mängder energier mellan kvarkar och leptoner. Elementarpartiklarna kvarkar, leptoner och gluoner är alla inkluderade i den grundläggande teorin inom partikelfysik, Standardmodellen.

En metod för att studera elementarpartiklar och deras egenskaper är att accelerera atomkärnor i så kallade partikelacceleratorer till en väldigt hög hastighet, vilket bidrar till att atomkärnorna blir högenergetiska, för att sedan kollidera med varandra. Kollisionerna ger upphov till att nya partiklar bildas och dessa partiklar detekteras och analyseras för att ge information om deras egenskaper och utvecklingen av förloppet precis efter kollisionen. Atomkärnor består av protoner och neutroner, vilka ingår i gruppen hadroner som består av kvarkar och gluoner i dess bundna tillstånd. När högenergetiska atomkärnor med ett högt proton- och neutron-innehåll kolliderar uppstår ett tillstånd där materia har väldigt hög densitet och temperatur. Detta tillstånd kallas Kvark-Gluon-Plasma och kan ha existerat under en kort period precis efter universums födelse, the Big Bang. När tillståndet Kvark-Gluon-Plasma uppstår har kvarkarna och gluonerna en större rörelsefrihet än i deras bundna tillstånd. En viktig del rörande forskning inom partikelfysik är att få förståelse för den frihet att röra sig utanför sina bundna tillstånd vilket kvarkar och gluoner erhåller vid höga densitet och temperatur.

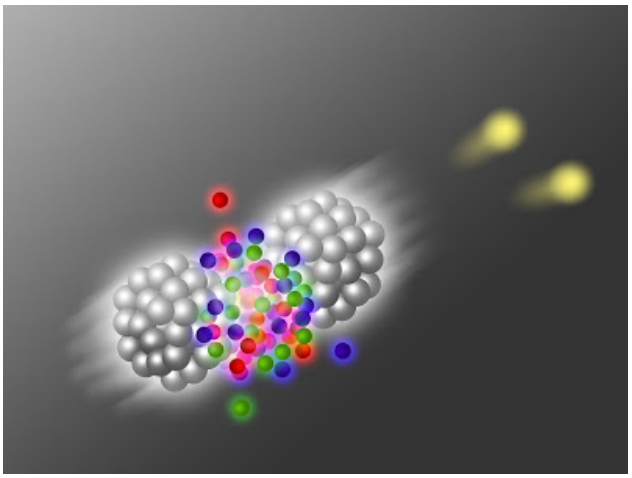

Figure 0.1: Två kolliderande atomkärnor som ger upphov till att nya partiklar bildas[1].

Livstiden för tillståndet Kvark-Gluon-Plasma som kan skapas i dagens laboratorium är väldigt kort vilket gör tillståndet omöjligt att detektera direkt. För att erhålla information om tillståndet och bekräfta dess existens studeras olika signaler genererade av Kvark-Gluon-Plasman. I den här uppsatsen har en av dessa signaler analyserats, så kallat elliptiskt flöde. Benämningen flöde kan härledas från att Kvark-Gluon-Plasman kan bete sig som en vätska. När Kvark-Gluon-Plasma expanderar minskar även dess densiteten och temperaturen vilket bidrar till att nya hadroner bildas. Genom att mäta olika utfall av partikelproduktionen, till exempel hur de flödar, kan nya kunskaper om Kvark-Gluon-Plasman erhållas. I uppsatsen används data från ALICE-experimentet vid forskningslaboratoriet CERN. Data har framtagits genom kollisioner av blykärnor i världens största partikelaccelerator, the Large Hadron Collider (LHC).

Contents

1 Introduction

The study of strongly interacting matter at high energy densities is today possible by colliding heavy ions at relativistic energies. In these collisions a new form of matter, *Quark-Gluon Plasma* (QGP), can be observed[2]. This highly energetic state of matter is believed to have existed in the early universe, a few microseconds after the Big Bang. In this state the fundamental particles, quarks and gluons, are no longer confined within their hadronic bound states, and an opportunity is given to study the fundamental theory of the strong interaction, Quantum Chromodynamics, which governs the properties and interactions of these particles under new circumstances.

In this thesis one of the detectable signals generated by the QGP is studied. The signal under study is referred to as *elliptic flow* and it provides information regarding the anisotropic expansion from real space to momentum space that occurs in mid-central relativistic heavy-ion collisions. The aim of this thesis is to extract and study the elliptic flow parameter v_2 of pions, protons, kaons and ϕ mesons as a function of transverse momentum p_T. Further, a constituent-quark number scaling of the elliptic flow as a function of the transverse kinetic energy EK_T is performed for all identified particles. At the present time, the state of QGP and its properties are not yet completely understood. However, there are theories that are in good agreement with experimental data today, attempting to explain the evolution of the system created in the relativistic heavy-ion collisions. In this thesis the results of the elliptic flow $v_2(p_T)$ and the scaling properties for the identified particle species will be analyzed by the support of both the ideal hydrodynamic[3] and the quark recombination models[4, 5].

2 Theory

In this section an introduction of two related theories, *the Standard Model* of particle physics (SM) and *Quantum Chromodynamics* (QCD), is presented. The SM describes matter on a level of fundamental particles, and QCD - the strong interactions between these particles. For a more complete overview of the SM and QCD see Ref. [6] and Ref. [3, 7], respectively. Further, this section briefly describes resonances, which are hadrons decaying via strong interactions, as well as the invariant mass of particles. Finally, the concept of Quark-Gluon Plasma (QGP) is introduced. Resonances and invariant mass are more extensively discussed in Ref. [6] and QGP in Ref. [3, 7].

2.1 The Standard Model

The Standard Model aims to explain the properties of fundamental particles and their interactions, which are governed by fundamental forces. The theory divides the fundamental particles into two groups, *bosons* and *fermions*, characterized by their intrinsic spin. Bosons and fermions hold integer-spin and half-integer-spin, respectively. All known matter is made up of fermions, and the interactions between the fermions are governed by four fundamental forces: the strong force, the weak force, the electromagnetic force, and the gravitational force. Each of the strong, weak and electromagnetic forces have their own corresponding boson, which is a fundamental particle that acts as a force mediator. Fermions interact with each other by transferring four-momentum, and that transfer is carried out by the bosons. A force mediator for the gravitational force has not yet been discovered, and thus it is only a theoretical prediction at the present time. Due to the fact that no quantum theory exists for gravity, it is not included in the SM.

There are 12 fermions, each with their own respective antiparticle, in the SM and these particles can be divided into two subgroups: *quarks* and *leptons*. The subgroup of quarks consists of six different flavors: up (u), down (d), charm (c), strange (s), top (t), and bottom (b). The quarks are paired in three generations, where the first generation consists of the lightest quarks, u and d, that make up stable matter. The second and third generations consist of heavier quarks and form unstable matter. The three generations can be viewed in Fig. 2.1. Quarks have both color and electric charge. The color charge confines the quarks within

hadrons and thus quarks cannot be observed as individual particles. Hadrons consist of quarks and gluons, collectively referred to as partons, and there are two types of hadrons: *mesons* and *baryons*. Mesons consist of a quark and an antiquark, and baryons of three quarks. The six remaining fermions are leptons and they are also arranged in pairs and three generations: the electron and the electron neutrino, the muon and the muon neutrino, and the tau and the tau neutrino. The three neutrinos are electrically neutral, whereas the electron, the muon and the tau all have electric charge.

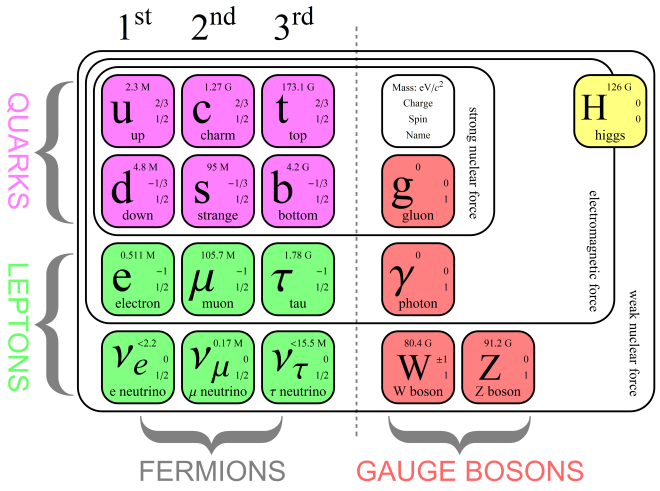

Figure 2.1: An overview of the three generations of fermions and the force mediating bosons in the Standard Model is presented[8].

Bosons are mediators of the strong, weak and electromagnetic forces. The mediators of the electromagnetic force are *photons*, which are massless and electrically neutral, and they interact with electrically charged particles. Interactions carried out by photons are elaborated upon in the theory of Quantum electrodynamics (QED). The $W^{\pm}$ and Z^0 bosons mediate weak interactions between both quarks and leptons. These bosons are massive and the $W^{\pm}$ bosons carry electric charges, whereas the Z^0 boson is electrically neutral. The strong force is mediated by *gluons*, which are massless bosons that carry color charge. The gluons interact with color charged particles, i.e. quarks and gluons.

2.2 Quantum Chromodynamics

Quantum chromodynamics (QCD) is the theory that describes the strong interactions between color charge particles. Analogously to QED, QCD describes interactions that are mediated by massless spin-1 bosons that couple to conserved charges. The conserved charges for QCD are called color charges. The quarks can carry red, blue and green charge, while the anti-quarks carry anti-red, anti-blue and anti-green. The gluons carry a combination of color and anti-color charges. Even though QCD has not been tested quite as extensively as QED, the theory is in good agreement with a large amount of experimental data. The major difference between the two theories emerges from gluons being able to self-interact, which photons cannot[3]. The gluon-gluon interactions are possible due to gluons themselves carrying color charge, and these interactions give rise to two important properties within the theory of QCD: *color confinement* and *asymptotic freedom*.

The color confinement requires that systems of quarks and gluons can only be observed in a color-neutral state, i.e. having zero color charge[6]. Baryons have each of the three colors, while mesons have a color and an anti-color. However, it appears as if the quarks are relatively free to move around while confined within hadrons. This liberty to move as free particles inside the hadrons is due to asymptotic freedom,

which means that the strong interactions gets weaker at short distances[7]. The strong force typically acts at a distance of order 1 fm, which is approximately the radius of a proton, and the strength of the strong interaction is illustrated by the strong coupling constant α_s, which is often referred to as the running coupling constant due to its variation associated with distance and momentum. Due to asymptotic freedom, the strong coupling constant α_s decreases with decreasing distance. Short-distance interactions, within the asymptotic freedom range ≤ 0.1 fm, are associated with large momentum transfer between the interacting particles. This means that the strong coupling constant, besides distance, also decreases with increasing momentum. Quantum fluctuation is a process where a particle can be converted into two or more particles for a short period of time[6]. Similarly to the photon in QED, virtual quark-antiquark pairs tend to screen the color charges. However, in QCD the quantum fluctuation process enables gluons to emit and absorb new gluon pairs, leading to anti-screening of the original color charge and thus the interactions diminish at short distances. The effect of anti-screening prevails over screening, hence asymptotic freedom is expected at short distances.

Baryons and mesons consist of three and two quarks, respectively, and these quarks are referred to as valence quarks. However, hadrons do not only consist of valence quarks but also of sea quarks, antiquarks, and gluons, and they are all confined within the hadrons. It is the valence quarks that carry the larger part of the hadron momentum while the residual composition carries the smaller part.

2.3 Resonances and invariant mass

There are many types of hadrons but only the proton is stable and thus the majority will decay within a short period of time. The dominant process, due to the large coupling constant, is decay via the strong force. If this process is not possible, unstable hadrons will decay by electromagnetic or weak interactions. Depending on the lifetime of the hadrons, they are referred to as *long-lived* or *short-lived*, where short-lived hadrons have a lifetime of $\sim 10^{-23}$s[6].

Hadrons that decay via strong interactions are generally referred to as *resonances* and they are too short-lived to be directly observed[3]. Thus, their existences must be deduced from observations on their decay products, i.e. more stable (or long-lived) hadrons. The ϕ meson is composite of the quark-antiquark pair $s\bar{s}$ and has a lifetime of $(1.55 \pm 0.01) \times 10^{-23}$s[9], thus even when created in high energy collisions (and hence being a relativistic particle) it only travels a very short distance before decaying. Consequently, the ϕ meson does not reach any detector before decaying and the decay products are measured instead. A method used in order to achieve information about short-lived particles is to observe the invariant mass distribution of the decay products. By doing so the mass of the mother particle can be determined and other properties like the momentum p may be determined as well. The invariant mass, also referred to as the rest mass, of a particle is a property that remains constant in all frames of reference related by Lorentz transformations. Hence, the mass m of a particle in its rest frame is equal to its invariant mass, which can be calculated by measuring the momentum p and energy $E = \sqrt{pc^2 + (mc^2)^2}$ of the particle in any frame. The invariant mass m is defined, via the energy-momentum relation, as

$$m^2c^2 = \left(\frac{E}{c}\right)^2 - \vec{p}^2 \tag{2.3.1}$$

By a small alteration of the previous definition (Eq .2.3.1), the invariant mass m_{inv} of the mother particle, in a two-body decay, can be determined as follows

$$m^2c^2 = \left(\frac{E_1 + E_2}{c}\right)^2 - \left(\vec{p_1} + \vec{p_2}\right)^2 \tag{2.3.2}$$

where the respective energy E and momentum p of the two decay products is designated by the indices 1 and 2.

2.4 Quark-Gluon Plasma

Quark-gluon plasma (QGP) is a near to thermalized state of quarks and gluons, meaning that the quarks and gluons, in this state, are free to move across a volume larger than a hadron[3]. Thus, the QGP is a state where the strongly interacting matter is deconfined. The ordinary state of quarks is to be confined in hadrons, due to the color confinement of QCD. However, at high enough energy or particle density the hadrons effectively dissolve. The quarks inside individual hadrons will find - at a distance less than the hadron radius - a number of quarks that are not of the original hadron composition and hence the quarks are no longer able to identify their original partners. Thus the quarks and gluons are said to be deconfined in this high particle density state of matter, known as the QGP. The same process occurs at high temperatures: when the temperature increases in a nuclear matter system, low mass hadrons, mostly pions, are created[3]. Consequently, the particle density in the system will increase and as a result at high enough energy the quarks and gluons are said to be deconfined, and thus a phase transition into the state of QGP occurs.

In the very early universe, during the first few microseconds after the Big Bang, the QGP is believed to have existed[7]. In the present day, the QGP may exist at the centre of neutron stars, which have a relatively low temperature but high particle density. Furthermore, the QGP state can be created briefly by powerful particle accelerators colliding heavy ions. In these highly energetic heavy-ion collisions, the energy density is high enough to create a fireball, which dissolves the nuclei into a QGP state. After its creation, the fireball will rapidly expand under its own pressure and thus the density and temperature of the fireball decreases, this is referred to as the freeze-out phase. During the freeze-out phase, the temperature eventually decreases until the partons can no longer be in the state of QGP and thus begin to hadronize, meaning that the individual partons combine into hadrons.

The lifetime of the QGP created in heavy-ion collisions is short, after only about 10^{-22} s the matter starts to hadronize[10]. As the QGP has a short lifetime it is impossible to study the phenomena directly; instead different signals generated by the QGP are observed. Signals of the QGP are essential to study in order to understand the intrinsic properties of the QGP. The very existence of the QGP is manifested through signals such as J/Ψ suppression, strangeness enhancement, electromagnetic probes, jet quenching and anisotropic collective flow[3]. The signal of QGP treated in this thesis is one type of anisotropic collective flow called elliptic flow. A brief overview of the signal is given in Sec. 3.6.

3 High-Energy Nuclear Physics

High-energy nuclear physics is an interdisciplinary field in which particle and nuclear physics overlap. High-energy particle physics treats single particles, such as leptons, quarks and hadrons, and the interactions between these particles. Nuclear physics extends to nuclei and their interactions, and the collision action of moving fundamental particles. In high-enery nuclear physics, these fields intersect and the properties of hot and dense hadronic matter are analyzed through fundamental interactions. This section will give a brief overview of the field and some of its observables, which are used in order to analyze different phases of the hadronic matter created in the collisions. For a more complete overview of relativistic heavy-ion collisions and their observables see Ref. [3, 7]. Further, anisotropic collective flow is discussed and more details on the topic is given by Ref. [7, 11]. At the end of the section, two models: *ideal hydrodynamics* and *quark recombination*, are briefly discussed. A more extensive description of the models is given by Ref. [3] for the ideal hydrodynamics model and Ref. [12] for the quark recombination model.

3.1 Relativistic heavy-ion collisions

The goals of relativistic heavy-ion collisions is to study the properties of matter at high energies[7]. The large amount of energy involved is an important characteristics in relativistic heavy-ion collisions. The energy

densities in these collisions are very high due to a large quantity of energy,$\sim$ 1000 TeV, being distributed over a small region of space, $\sim$ 100 fm^3, during a very short period of time, $\sim 1 - 10$ fm/c. The high energy density produced in the collision may give rise to new forms of matter such as the QGP described in Sec. 2.4.

The center-of-mass energy is the energy available to produce new particles in the collisions and it is much larger than individual hadron masses in relativistic collisions at the LHC. Thus in these collisions large particle multiplicities are produced, meaning that the number of particles produced in the collision is much greater than the initial number of nucleons, in particular for central collisions. Gold and lead consist of a large number of nucleons and they are commonly used as the colliding species. The particles produced in the collision can be treated as a large macroscopic system, hence theories such as thermodynamics, hydrodynamics, and field theory at finite temperature and density can be used to describe the system[7]. However, a hydrodynamic or statistical approach to estimate the effects in the systems is not sufficient since the systems are not static. By combining different theories, such as relativistic hydrodynamics and quark recombination models, the interpretations of the effects in the systems can be improved.

3.2 Participants, spectators and collision centrality

In a relativistic nucleus-nucleus collision the nucleons of each nucleus propagate along parallel trajectories and the direction of the beam lines usually defined as the z-axis. The nucleons appear as two thin pancakes before the collision due to Lorentz contraction, which only happens in the direction of motion and arises from relativistic effects. The nucleons that interact in the collision are referred to as *participants* and the nucleons that do not interact are referred to as *spectators*, see Fig. 3.1. Inelastic nucleon-nucleon collisions is the dominant process for the participants and the hadron interactions in this process characterize the collision as soft or hard[13]. A hard collision gives rise to jets, highly energetic hadron and heavy quarks due to the partons that interact, carry and transfer a large fraction of momentum. In a soft collision a low amount of momentum is transferred by color fields, thus the strong coupling constant becomes large and the strong interaction is dominant. A soft collision results in a formation of quarks, antiquarks and gluon pairs[14].

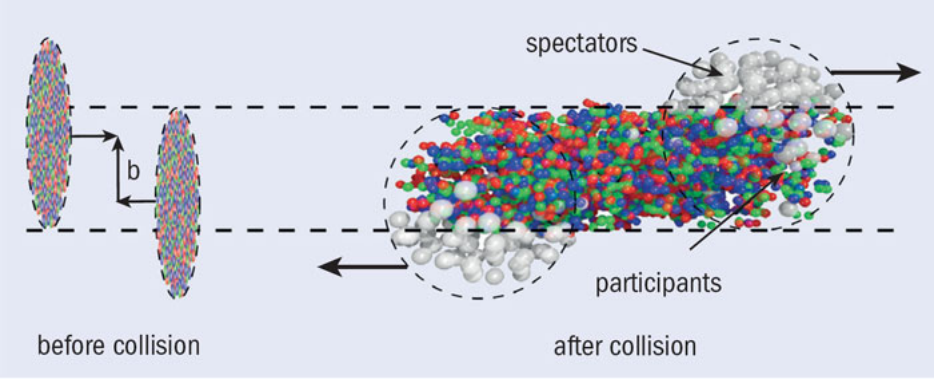

Figure 3.1: The initial state, before the collision, represents the contraction of the nuclei and the impact parameter b. The finial state, after the collision, represents the spectators and the participants[15].

The impact parameter b (see Fig. 3.1) is the length of a two-dimensional vector called the impact vector. The impact vector is in the plane perpendicular to the beam line direction and its length corresponds to the distance between the centers of the two colliding nuclei. The value of the impact parameter b cannot be measured directly, instead experimental observables can be used in order to determine its value, e.g. particle multiplicity, transverse energy[5]. *The collision centrality* depends on the impact parameter b, where a low or high value of b corresponds to a central or peripheral collision, respectively. Hence high particle

multiplicity or high transverse energy events come from central collisions and low particle multiplicity or low transverse energy events come from peripheral collisions[3]. The centrality of a collision is usually expressed as the percentage of nuclear interaction cross section, where a low collision percentile represents a central collision. Contrarily, a high collision percentile represents a peripheral collision.

3.3 Transverse momentum and transverse mass

The transverse momentum p_T is the momentum of a particle perpendicular to the beamline direction, which as previously mentioned usually defines the z-axis. Using the z-axis as the beamline direction, the transverse momentum p_T is thus defined as

$$p_T = \sqrt{p^2 - p_z^2} \tag{3.3.1}$$

The transverse momentum is an important observable as it indicates how much the reconstructed particles were scattered in the collision. Hence, a hard partonic collision gives more high p_T particles whereas a soft partonic collision more low p_T particles.

The transverse mass m_T of a particle is its mass and momentum perpendicular to the direction of motion. Along this direction, which is the direction of the beamline and defines the z-axis, the transverse mass of the particle is invariant under Lorentz boost (relative motion with a constant velocity). The transverse mass m_T is, in natural units, defined as

$$m_T = \sqrt{m^2 + p_T^2} \tag{3.3.2}$$

where m is the mass of the particle and p_T its transverse momentum.

3.4 Rapidity and pseudorapidity

At relativistic energies, an alternative to standard velocity, *the rapidity*, is frequently used. The rapidity y is defined as

$$y = \frac{1}{2}\ln\left(\frac{E + p_z}{E - p_z}\right) \tag{3.4.1}$$

where $E = \sqrt{m^2 + p^2}$ is the total energy of the particle and m and p its mass and momentum, respectively. The momentum of the particle in the z-direction is denoted as p_z. The rapidity of a particle is a measurement of its momentum in the z-direction and it has the advantage of being additive for a Lorentz boost along the beam axis. The central rapidity region is the region in the center-of-mass frame where the rapidity $y \approx 0$. This region is of great interest due to the particles with a rapidity close to zero are either new particles produced in the collisions or particles of the beam that undergo scattering processes and hence changing their initial longitudinal momentum, i.e. the momentum along the beam axis[7].

In order to determine the rapidity of a particle, both the energy and the total momentum are needed. At relativistic energies, the total momentum and the relativistic mass of a particle can be difficult to measure precisely. However, to avoid this problem *the pseudorapidity* can be measured instead. The pseudorapidity η depends only on the angle θ between the three-momentum vector of the particle and the beam axis. The pseudorapidity is defined as

$$\eta = \frac{1}{2}\ln\left(\frac{|\vec{p}| + p_z}{|\vec{p}| - p_z}\right) = -\ln\left(\tan\frac{\theta}{2}\right) \tag{3.4.2}$$

For highly relativistic particles, the p_T of a particle is much larger compared to its mass and the pseudorapidity converges to the definition of rapidity, thus $y \approx \eta$.

3.5 Anisotropic collective flow

The azimuthal momentum space anisotropy of emitted particles can be observed in order to study the properties of a system produced in a heavy-ion collision. If the system established equilibrium after the collision it will undergo a collective expansion followed by hadronization. The collective expansion of the system is referred to as *the collective flow*. The collective flow is an important observable as it provides information about the evolution of the system right after the collision. Direct expansion and anisotropic expansion are two types of expansion included in the term collective flow. The elliptic flow, which will be treated in this thesis, is the most dominant contribution to anisotropic flow[15].

The reaction plane is spanned by the impact vector $\vec{b}$ and the direction of the beamline. The azimuthal momentum distribution of the particles with respect to the symmetry plane angle Ψ_n can be characterized by the Fourier expansion[15]

$$E\frac{d^3N}{d^3p} = \frac{d^2N}{2\pi p_T dp_T dy}[1 + \sum_{n=1}^{\infty} 2v_n \cos(n(\varphi - \Psi_n))] \tag{3.5.1}$$

where N is the number of particles, p the momentum, φ the azimuthal angle, p_T the transverse momentum and y the rapidity. The n^{th} Fourier coefficient is v_n, which is commonly referred to as harmonic or anisotropy parameter, and Ψ_n the n^{th} order of the symmetry plane angle. The sine term in the expansion vanishes due to the symmetry with respect to the reaction plane Ψ_{RP}. The Fourier coefficients v_n are calculated by the following equation

$$v_n = \langle \cos[n(\varphi - \Psi_n)] \rangle \tag{3.5.2}$$

Each one of these harmonics v_n corresponds to a different type of anisotropy[5]. The first harmonic v_1 is called direct flow and it represents the average change of the momentum distribution in the transverse plane. The second harmonic is the elliptic flow parameter v_2 and it indicates the azimuthal anisotropy of the momentum distribution. The third harmonic v_3 is called the triangular flow and it reflects a triangular shape of the medium created in the collision.

3.6 Elliptic flow

To achieve high elliptic flow in a heavy-ion collision the shape of the impact region, which depends on the impact parameter b, in the reaction plane should be asymmetric or almond shaped, see Fig. 3.2. The asymmetric shape is an important property for the development of elliptic flow as the interacting particles in this asymmetric region produce momentum anisotropy. Central head-on collisions, with an impact parameter b close to zero, generate low elliptic flow due to the symmetric shape of the impact region. A very peripheral collision with a very high value of b results in an asymmetric impact region but the impact region is however small and thus also results in low elliptic flow. Hence, mid-central collisions generate maximum elliptic flow.

Out-of-plane flow usually occurs at lower energies. This is manifested by the elliptic flow being negative, which indicates that the largest momentum transfer takes place in the plane perpendicular to the reaction plane. At higher energies, in-plane flow is more common and the elliptic flow is then positive implying that the largest momentum transfer occurs in the reaction plane. This energy dependence of elliptic flow can be interpreted as an effect generated by spectators[7]. The spectators are blocking the expansion in the reaction plane at lower energies, thus the matter is forced to expand out of the reaction plane. At higher energies the spectators move fast and thus the matter can expand in the reaction plane.

The non zero elliptic flow produced in an asymmetric impact region can most easily be interpreted by a hydrodynamic model. The first result of elliptic flow produced at the Relativistic Heavy Ion Collider (RHIC) at Brookhaven National Laboratory indeed indicated that elliptic flow approaches the prediction of a perfect liquid[7]. The hydrodynamic model of elliptic flow is a signature that the system undergoes a

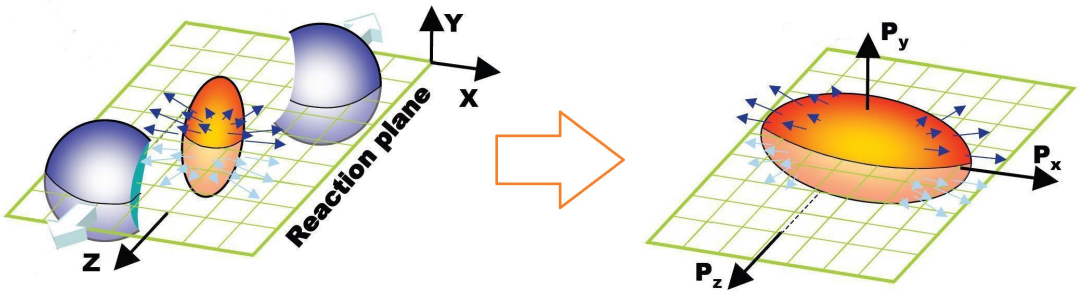

Figure 3.2: A schematic illustration of the almond shaped impact region in the reaction plane, after a non-central collision, as it evolves into anisotropic expansion in momentum space[16].

very fast thermalization, which is one of the strongest proof of the existence of the QGP. If the system did not undergo thermalization, a collective flow could not occur.

3.7 The ideal hydrodynamic model

There are different models to describe the behavior of elliptic flow produced in relativistic heavy-ion collisions. The development of elliptic flow as a function of p_T can be divided into three different regimes: low ($p_T \lesssim 2.0$ GeV/c), intermediate ($2.0 < p_T \lesssim 5.0$ GeV/c) and high ($p_T \gtrsim 5.0$ GeV/c)[4]. The ideal hydrodynamic model is a good approach to describe the behavior of elliptic flow in the low p_T regime and calculations of the model predict a mass ordering of $v_2(p_T)$[5]. It has been observed that the QGP behaves like a nearly perfect liquid[17] and this can be described by the ideal hydrodynamics model in the low p_T regime. This thesis will treat the elliptic flow as a function of p_T up to p_T=3.6 GeV/c.

The system produced in a relativistic heavy-ion collision undergoes different stages, which can broadly be divided into the pre-equilibrium, expansion, hadronization, and freeze-out stage. In the pre-equilibrium stage a fireball is produced by the initial partonic collisions. The fireball is initially highly excited and not in equilibrium. Instead local equilibrium can be established by parts of the system colliding at a high frequency. When local equilibrium is established, the system is in a locally thermalized state. In relativistic heavy-ion collisions local equilibrium is rapidly established in the produced fireball and this period of time is referred to as the thermalization time. In the expansion stage, the system undergoes expansion due to the gradient force acting upon it. When the system expands, the energy density decreases and hence the temperature also decreases. If a QGP phase transition has occurred in the collision the partons will start to form hadrons due to the decreasing energy density, thus the system enters the hadronization stage. Eventually all the partonic matter is converted into hadronic matter. The hadronic matter may also establish local equilibrium by the constituent hadrons of the system colliding frequently. Hence the system continue to expand and the temperature decreases further. The last stage, freeze-out, is a sequence of two stages: chemical and kinetic freeze-out. In the chemical freeze-out, local equilibrium is still maintained due to elastic collisions. However, the rate of inelastic collisions, which makes it possible for hadrons to change their identities, becomes low compared to the expansion rate. Hence the hadron abundances is fixed after this stage. The kinetic freeze-out occurs when the average distance between the hadrons is larger than the range of the strong interaction and the collision frequency is not high enough to maintain local equilibrium. In the kinetic freeze-out stage, the hydrodynamic description will no longer be valid. The hadrons in the kinetic freeze-out stage are decoupled and then the long-lived hadrons can be observed in the detectors[3].

The previously discussed stages give a simple overview of the ideal hydrodynamic model used to describe a system produced in relativistic heavy-ion collisions. The ideal hydrodynamic model is in good agreement with a variety of experimental data, albeit problems with the model still remain[3]. The model is insufficient as a description for more peripheral collisions. It is also incompatible with experimental data regarding elliptic flow at high values of transverse momentum, where the ideal hydrodynamic model predicts increasing elliptic flow with increasing transverse momentum.

3.8 Quark recombination models

For $p_T \gtrsim 2.0$ GeV/c the hydrodynamic model is in disagreement with experimental data due to the model predicting increasing v_2 with increasing p_T[5]. For higher p_T quark recombination models can be applied to explain the properties for the evolution of the system produced in relativistic heavy-ion collision. The mechanism of the hadronization stage of the system can be explained by these models, which has been developed due to observed irregular enhancement of baryons and the *constituent-quark number scaling* (CQNS) of elliptic flow[12]. The quark recombination models suggest that part of the collective flow originates from the transition of partonic matter to hadronic matter, i.e. the hadronization phase. The main idea of the models is that the quarks coalescence into hadronic bound states similar to nucleons into nuclei[12].

The quark recombination models can be used for describing $v_2(p_T)$ in the intermediate range ($2.0 < p_T \lesssim 5.0$ GeV/c) and as previously mentioned, the models can be applied at the hadronization transition to explain the outcome of CQNS. The CQNS is a scaling property of the elliptic flow, $v_2(p_T)$, and its properties are believed to emerge from quarks and antiquarks being recombined into hadrons in a collectively moving medium. This can be interpreted as a universal elliptic flow of the quarks and antiquarks in the hadronization phase[18].

4 The ALICE Experiment at the Large Hadron Collider

A Large Ion Collider Experiment (ALICE) is an international experimental collaboration that studies collisions at the Large Hadron Collider (LHC). The LHC is situated at the European Organization for Nuclear Research (CERN) near Geneva, Switzerland. In this section the ALICE experiment and some of its detectors are introduced. The detectors used for the particle identification (PID) in this thesis are *the Time Projection Chamber* (TPC) and *the Time-Of-Flight detector* (TOF) and for a more complete overview of these detectors see Ref. [19]. Further, information on the collision centralities used in this thesis is provided by the V0 detector, which is extensively discussed in Ref. [20].

4.1 The Large Hadron Collider

The LHC is the largest and most powerful particle accelerator in the world and it is the latest addition to CERN's accelerator complex[21]. The LHC is constructed to collide protons and heavy-ion beams, which are travelling close to the speed of light. The main components of the LHC are two synchrotron rings, situated $\sim$100 m underground, and both rings have a circumference of 26.7 km. The rings traverse the Swiss/French border and consist of superconducting magnets and accelerating cavities, which boost the energy of the particle beams along the way. The protons and nuclei are pre-accelerated in a linear accelerator before entering the Proton Synchrotron and the Super Proton Synchrotron where they are accelerated further before being injected into the LHC-rings. This is where the beams are accelerated up to their collision energies.

The strong magnetic fields in the LHC ring are used for both accelerating the particles in the beams to high energies and also for keeping the beams focused. Further, the highly energetic beams of particles are brought to the experiments' designated intersection points where the beam collisions occur. These magnetic fields have during the LHC *Run 1* (2009-2013) achieved a center-of-mass energy of $\sqrt{s_{pp}} = 8$ TeV for

proton-proton (p-p) collisions, $\sqrt{s_{pN}} = 5.02$ TeV for proton-lead (p-Pb) collisions and $\sqrt{s_{NN}} = 2.76$ TeV for lead-lead (Pb-Pb) collisions. In March 2015 the LHC *Run 2* started after a two year technical stop. During the two year stop the magnets have been upgraded in order to run at energies almost twice as high than in the first run. In Run 2 center-of-mass energy of $\sqrt{s_{pp}} = 13$ TeV for proton-proton collisions and $\sqrt{s_{NN}} = 5$ TeV for the lead-lead collisions have been achieved[22].

There are four locations around the LHC where the beams are made to collide for experimental observations. These colliding locations correspond to the four main experiments at the LHC: CMS, LHCb, ATLAS and ALICE. The data used in this thesis was collected by ALICE in 2010.

4.2 The ALICE experiment

The ALICE experiment is dedicated to the study of the physical properties of QCD at high energy density and temperature in lead-lead collisions. The physics programme at ALICE also includes the study of strongly interacting matter in proton-proton collisions and of cold nuclear matter effects in proton-nucleus collisions. The ALICE apparatus, see Fig. 4.1, consists of 18 different detector systems that can be divided into three categories: central barrel detectors, forward detectors, and the MUON spectrometer[19].

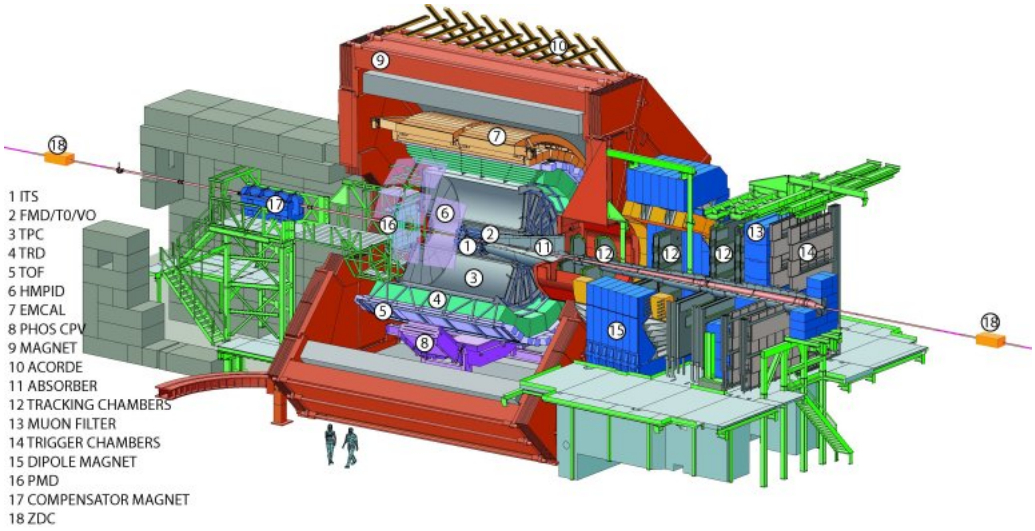

Figure 4.1: An overview of the 18 different detectors in the ALICE experiment[23].

The 10,000 tonne ALICE detector is located 56 m underground and it is in total 26 m long, 16 m high, and 16 m wide[24]. The central barrel detectors include the Time Projection Chamber (TPC), Inner Tracking System (ITS), Transition Radiation Detector (TRD), Time Of Flight (TOF), Photon Spectrometer (PHOS), Electromagnetic Calorimeter (EMCal), and High Momentum Particle Identification Detector (HMPID). The TPC surrounds the ITS, which is located closest to the beam pipe. They are both tracking detectors used for tracking and to identify charged particles. The central barrel region is enclosed within a solenoidal magnet that generates a magnetic field of 0.5 T[19]. The tracking detectors measure the momentum of the particles by observing their trajectories as they are bend by the magnetic field. The ITS improves the momentum resolution of the tracks measured by the TPC. It also gives a more precise radial and azimuthal determination. The main purpose of the ITS is to identify the weakly decaying heavy particles by determining, with high precision, the collision vertex and locating the secondary vertices. The EMCal and PHOS measure the total energy of electrons and photons as they interact with multiple layers of matter resulting in the particles energies being absorbed. EMCal has a significantly larger acceptance than PHOS, while PHOS has a

significantly better energy resolution than EMCal. The HMPID detects fast-moving particles and the TRD electrons. The TOF determines the particles flight time from the collision point to the detectors location[23].

Some of the ALICE forward detectors are the Photon Multiplicity Detector (PMD), the Forward Multiplicity Detector (FMD) and the quartz Cherenkov detector T0. The PMD measures photons and the FMD charged particles. Information on the time and longitudinal position of the collision point are provided by the T0[19]. The V0 detector is also included in the ALICE forward detectors and this detector is important for the determination of the collision centrality. The MUON spectrometer measures the production of light vector mesons and is also used for identifying quarkonium.

4.3 The Time Projection Chamber

The Time Projection Chamber (TPC) is the main tracking detector in the ALICE apparatus and is used for particle identification and reconstruction of their trajectories in space. At the collision point the TPC will collect information on the flavor composition and the expansion in space-time of the created fireball. By combining information provided from the TPC, ITS and TRD, hadron resonances and hadrons composited of heavy quarks can be studied[25].

The TPC is located inside the central barrel of ALICE, it encircles the ITS and is surrounded by the TRD. The detector consists of a 88 m^3 gas filled hollow cylinder and the axis of the cylinder is aligned with the beamline from the LHC. The axis is also parallel to the solenoidal magnetic field in the ALICE detector. The device has an inner radius of 85 cm, an outer radius of 250 cm and a total length of 500 cm. At the ends of the cylinder Multi-Wire Proportional Chambers (MWPCs) are located. A conducting electrode, charged to 100 kV, is situated at the axial center and divides the cylinder into two drift regions. The gas in the chamber is a mixture of Ne, CO_2 and N_2 at atmospheric pressure. The gas is ionized when charged particles traverse the detector. The liberated electrons drift towards the end plates due to the electric field present in the detector. When the electrons reach the MWPCs their arrival times are detected. The drift time of the electrons can be measured by comparing the time of the collision, which is given by other detectors, and the arrival time at the MWPCs. The MWPCs determine the x-y components whereas the drift time and drift velocity reconstructs the z. Hence the trajectories of the charged particles in three-dimensional space can be determined with high accuracy[26].

The particle identification in the TPC is performed by measuring the particle's average energy loss per unit path length, $\langle \frac{dE}{dx} \rangle$. Charged particles lose their energies by ionization of atoms when moving through a gas. This specific energy loss is measured in the TPC and is well described by the Bethe-Bloch formula[27]. The TPC covers the full azimuthal angle and a pseudorapidity of $|\eta| < 0.9$. As mentioned previously, the magnetic field in the detector causes a curvature of the charged particle trajectories. The curvature of the trajectories is in the $x - y$ plane, that is the azimuthal plane, and it is used for determining momentum of the charged particles.

4.4 The Time-Of-Flight detector

The Time-Of-Flight detector (TOF) is used for identifying particles in the momentum range $\sim 0.5 - 4$ GeV/c. Particle identification by the TOF detector can be performed up to 2.5 GeV/c for pions and kaons, and up to 4 GeV/c for protons[19]. The TOF detector measures the flight time of the particles from the collision point to the detector and the start time at the collision is usually provided by the T0 detector. The travel time measured by the TOF detector and the momentum and path length measured by the tracking detectors can be used to calculate the particles masses. Measurements from the TOF and TPC detectors can be used for determining the particle ratio of pions, kaons and protons. Hence, combined results from the TOF and TPC provide information on the study of QCD thermodynamics and they are also used to determine the production of the open charm and the ϕ meson[28].

The TOF detector consists of a large array divided into 18 sections in the azimuthal direction. The sections are arranged in a cylindrical shape that encloses the ITS, TPC and TRD detectors. Each section is in turn divided into 5 modules along the beam direction and in total the modules contain 1638 detector elements, Multigap Resistive Plate Chamber (MRPC) strips[28]. The sections are situated 370-399 cm from the beam axis and cover full azimuth[19]. The TOF detector has a pseudorapidity range of $\mid \eta \mid < 0.9$ and the 18 sections cover an area of 160 m^2. The time resolution of the TOF is $\sim$100 ps.

For PID in TOF the measurements are usually presented by the velocity β as a function of momentum, which is measured by the TPC. The velocity β is the speed of an object v relative to the speed of light c and at relativistic energies it is convenient to express β, in natural units, as follows

$$\beta = \frac{p}{E} = \frac{p}{\sqrt{p^2 + m^2}} \tag{4.4.1}$$

where the p is the total momentum of the particle, with mass m, and E its total energy.

4.5 The V0 detector

The V0 detector is a small angle detector that provides trigger signals in the ALICE detector, such as a minimum bias trigger for the central detector and centrality trigger in lead-lead collisions. Additionally, it measures charged particle multiplicity, azimuthal distribution and beam luminosity. The measurement of the charged particle multiplicity and the azimuthal distribution are important to determine the collision centrality and the reaction plane, respectively[20].

The detector consists of two arrays called V0A and V0C. The two arrays consist of 32 plastic scintillating counters distributed in four rings, which in turn are divided in eight sections in the azimuthal direction. Every section of the V0A and V0C contains a counter that in total gives 64 channels. The channels measure charged particles and their arrival times. The thickness of the V0A and V0C counters are 2.5 cm and 2.0 cm, respectively. The V0A device is located at a distance of 330 cm from the interaction point in the positive z-direction and covers the pseudorapidity range $2.8 < \eta < 5.1$. The V0C device is located in the negative z-direction at a distance of 90 cm from the interaction point and covers the pseudorapidity range $-3.7 < \eta < -1.7$[20].

5 Analysis Method

In this thesis the aim is to study the elliptic flow of identified hadrons in Pb-Pb collisions at different centralities using the event-plane method and an invariant mass analysis. To measure the elliptic flow, the event-plane method is used to extract an approximation of the true reaction plane and thus relate the anisotropic momentum distribution of emitted particles to the estimated event-plane. Protons, pions and kaons can be identified through information extracted from the TOF and the TPC detectors. The ϕ meson can be identified through its dominant decay channel of two kaons and an invariant mass analysis. All the software in this analysis is written in the programming language C++ within the ROOT analysis framework[29].

5.1 Data from the ALICE experiment

The data used is from Pb-Pb collisions at the center-of-mass energy $\sqrt{s_{NN}} = 2.76$ TeV that was produced by the ALICE experiment in November 2010, more specifically the period LHC10h during Run 1. The data consists of events from four different collision centralities. The centrality intervals of the collisions are provided by the V0 detector. The number of events for each centrality is 653,186 for 10-20%, 1,355,734 for 20-40%, 2,090,233 for 40-60% and 2,099,822 for 60-80%. In total the data used consists of 6,198,974 events.

Each event contains a certain amount of tracks, from detected charged particles, and the track multiplicity for the different centralities is shown in Fig.5.1.

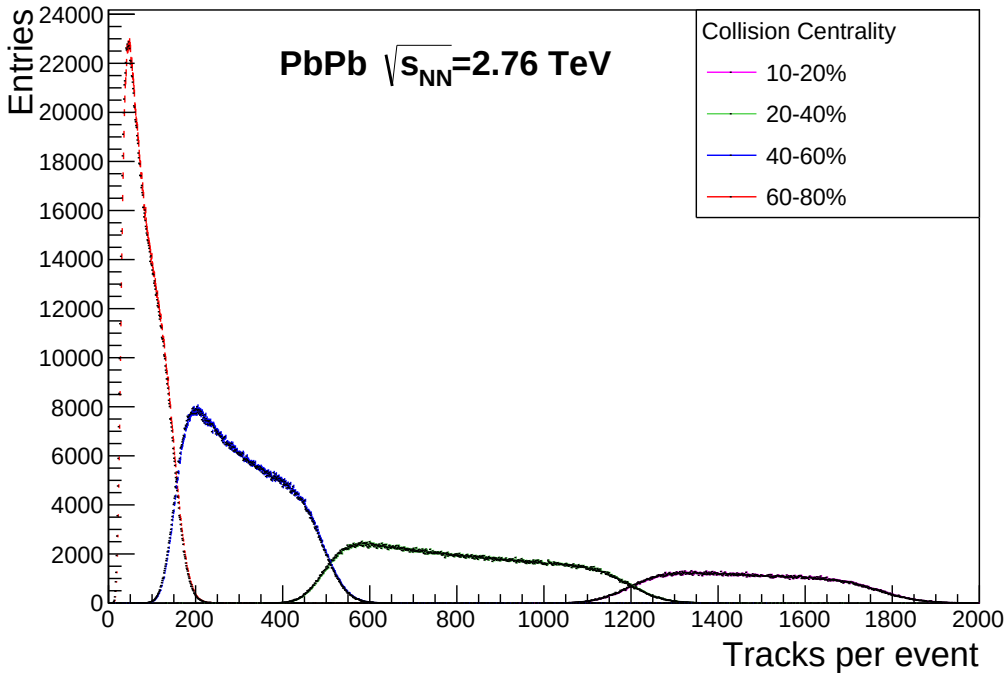

Figure 5.1: The number of TPC tracks of the different Pb-Pb collision centralities, determined by the V0 detector, used in this thesis.

5.2 The event-plane method

A method commonly used to estimate the elliptic flow coefficient v_2 is the event-plane method[30]. In this method an *event-plane* Ψ_{EP} is constructed by an estimate of the reaction plane Ψ_{RP}. Hence, an approximation of the true reaction plane can be obtained in each event. In an event the azimuthal distribution in momentum space of the particles is expressed as follows

$$\frac{dN}{d\varphi} \propto 1 + 2\sum_{j=1}^{N} v_n \cos[n(\varphi_j - \Psi_{RP})] \tag{5.2.1}$$

where N is the number of particles in the event and φ is the azimuthal angle of the particles. The n^{th} symmetry plane constructed by the reaction plane Ψ_{RP} can be estimated by the azimuthal angle distribution of particles. From Eq. 5.2.1 the event-plane Ψ_n can be obtained

$$\Psi_n = \frac{1}{n}\arctan\left(\frac{\sum_i \sin(2\varphi_i)}{\sum_i \cos(2\varphi_i)}\right) \tag{5.2.2}$$

The sum in the expression goes over all i particles used to determine the event-plane. The range of the event-plane is in $0 < \Psi_n < \frac{2\pi}{n}$. By estimating an event-plane all the particles under study in each event can

be related to this plane. In this thesis the elliptic flow coefficient v_2 is treated, thus n =2 in the equations above. For the event-plane determination particles in the transverse momentum range $0.5 < p_T < 3.0$ GeV/c are used. The particles used to define the event-plane cause a trivial correlation between the azimuth angle φ and the estimated event-plane Ψ_2 and this gives rise to an overestimate of the flow coefficient v_2. To avoid the autocorrelation effect the particles used for defining the event-plane are subtracted. The result of the autocorrelation effect can be observed, specifically at the p_T value 3.0 GeV/c, in Fig. 5.2.a. The autocorrelation effect causes an overestimate of the elliptic flow v_2 value. The result of removing the autocorrelation is displayed in Fig. 5.2.b, where a smoother curve can be observed as well as a slight decrease of the v_2 for all p_T values.

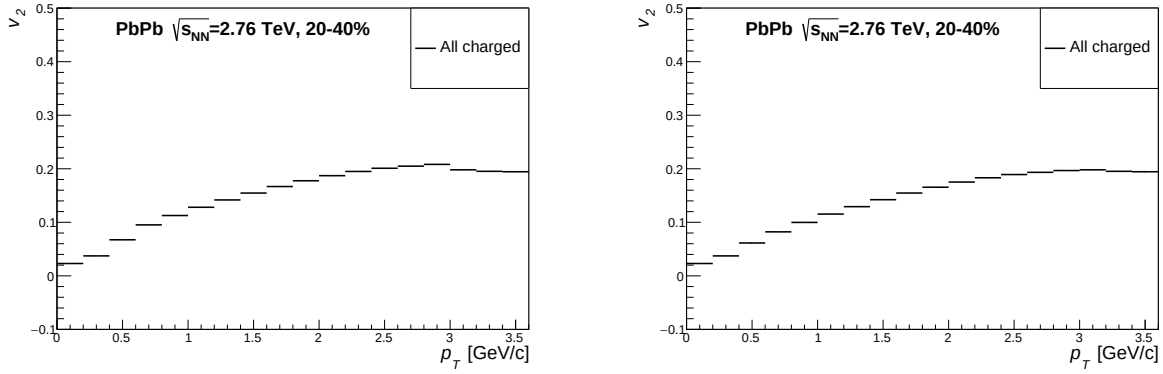

(a) Autocorrelation effect

(b) No autocorrelation effect

Figure 5.2: The elliptic flow v_2 as a function of p_T for all charged particles with the auto correlation effect is shown in (a). In figure (b) the autocorrelation has been removed.

5.3 Particle identification

The particle identification (PID) is performed by using information detected in the TOF detector:

$$\beta = \left(\frac{Track_{length}}{TOF_{time}} \right) / c \tag{5.3.1}$$

By studying the β distribution as a function of momentum p given by the TPC, distinctive bands arising from different particle species can be observed, see Fig. 5.3.a. The particles to identify are protons, pions and kaons. By inserting the particles respective mass in Eq. 4.4.1 and applying cuts the different particle species can be extracted. For each particle species i, Eq. 4.4.1 is

$$\beta_i = \frac{p}{\sqrt{p^2 + m_i^2}} \tag{5.3.2}$$

where the mass of protons, pions and kaons are 0.938 GeV/c^2, 0.140 GeV/c^2 and 0.494 GeV/c^2, respectively. The first condition for extracting pions was

$$\left| \beta - \beta_{pion} \right| < 0.017 \tag{5.3.3}$$

This symmetric cut was done over the entire p region. The extracted pion candidates are shown in Fig. 5.3.b. The first condition for extracting protons was

$$\left| \beta - \beta_{proton} \right| < 0.05 \tag{5.3.4}$$

The symmetric cut was done in the region $p \geq 2.0$ GeV/c where the bands of particle species start to overlap. For $p < 2.0$ GeV/c the distance between the proton and kaon bands was larger and thus easier to distinguish. Hence, an additional cut was made $\beta < \beta_{proton} + 0.02$ to achieve a cleaner proton sample. The extracted proton candidates are shown in Fig. 5.3.c. The first condition for extracting kaons was

$$-0.02+ < \beta - \beta_{kaon} < +0.01 \tag{5.3.5}$$

The reason for doing an asymmetric cut, in the region $p \geq 2.0$ GeV/c, was due to the distance between the kaon and proton bands being smaller than the distance between the kaon and pion bands. For the region $p < 2.0$ GeV/c an additional cut $\beta < \beta_{kaon} + 0.005$ was made as the band of kaons being more clearly distinguishable in this range and thus a cleaner kaon sample could be achieved. The extracted kaon candidates are shown in Fig. 5.3.d.

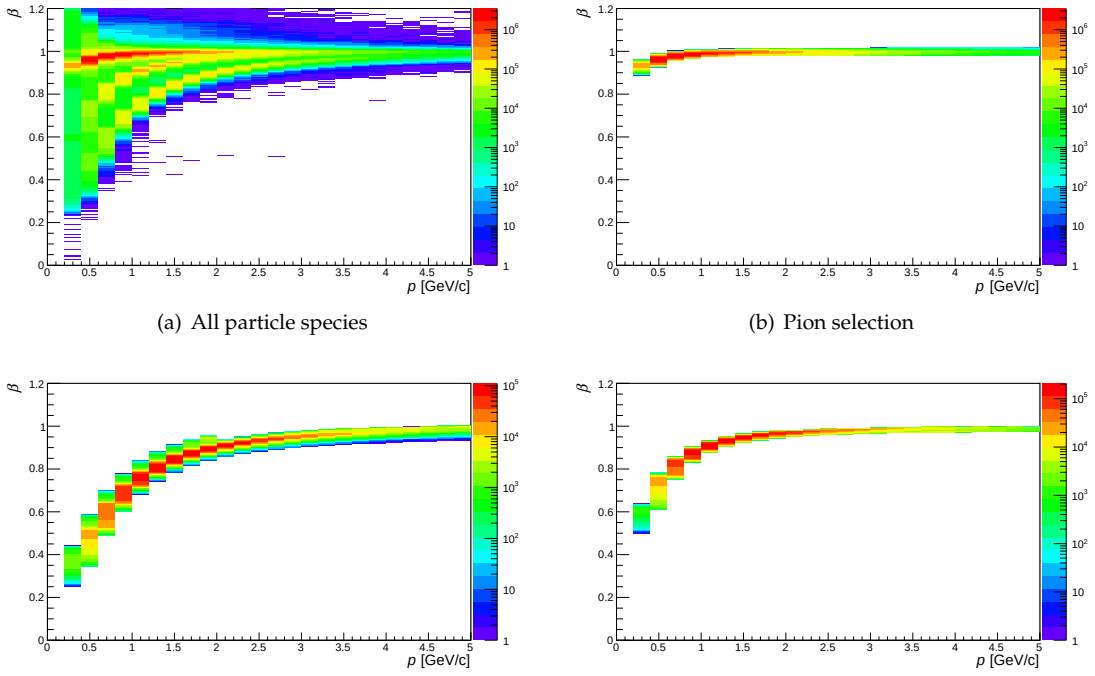

(a) All particle species

(b) Pion selection

(c) Proton selection

(d) Kaon selection

Figure 5.3: In (a) the β estimate distribution from the TOF detector is shown. The particle extraction of pions, protons and kaons is shown in (b), (c) and (d), respectively.

5.4 Extraction of elliptic flow for proton, pions and kaons

The first step to estimate the elliptic flow v_2 scaling is to calculate the correlation between the azimuthal angle φ of each charged particle and the reconstructed reaction plane. This is done by constructing the azimuthal distribution, with respect to the extracted event-plane ($\varphi - \Psi_{EP}$), as a function of the transverse momentum p_T. For each p_T bin, which has an interval of 0.2 GeV/c, a projection on the y-axis is done and then Eq.5.2.1 is inserted as a fit curve. For the p_T regions a clear sinusoidal modulation is expected if elliptic flow is present. A typical example of the sinusoidal modulation is shown in Fig. 5.4 and it is extracted from an interval $5.8 < p_T < 6.0$ GeV/c in 20-40% collision centrality for all charged particles. The elliptic flow parameter describes the size of the sinusoidal modulation and is expected to be largest for mid-central

collisions. For each p_T bin the elliptic flow parameter v_2 is extracted from the amplitudes of the sinusoidal modulation and plotted as a function of p_T. For each particle species under study the same procedure is carried out.

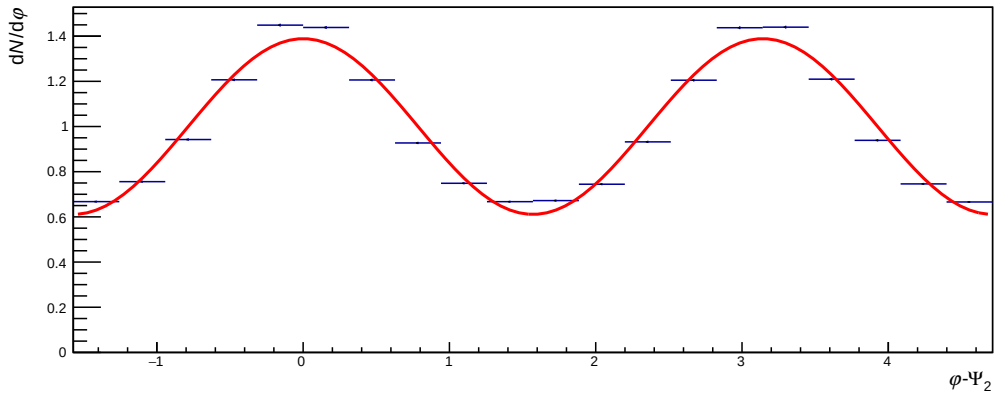

Figure 5.4: A clear sinusoidal modulation for all charged particles extracted from the interval $3.4 < p_T < 3.6$ in 20-40% collision centrality.

5.5 The ϕ meson and background estimation

To identify the ϕ meson, an invariant mass distribution needs to be obtained. If a signal is present, the invariant mass distribution will show a peak that corresponds to the invariant mass of the ϕ meson and hence a signal for the ϕ meson can be identified. The dominant decay channel of the ϕ meson is decaying to two kaons[7], K^+ and K^-, and this decay channel is used in this thesis to identify the ϕ meson. By assuming a K^+ and a K^- candidate originate from the same decay, the invariant mass distribution is obtained through combination of the momentum components and total energies of the two candidates.

The ϕ meson has a mass of about 1.019 GeV/c^2 and the kaon a mass of 0.494 GeV/c^2. The first step is to separate the kaons by charge and calculate their momentum components p_x, p_y and p_z, and also their total energies E. The information in the tracks detected consists of the transverse momentum p_T, the total momentum p and their azimuthal angle φ. Hence, the momentum components of the kaon and its total energy can be calculated. Each momentum component is obtained by the following equations

$$p_x = p_T \cos(\varphi) \tag{5.5.1}$$

$$p_y = p_T \sin(\varphi) \tag{5.5.2}$$

$$p_z = \sqrt{p^2 - p_T^2} \tag{5.5.3}$$

The total energy of the kaon is calculated by

$$E = \sqrt{m^2 + p^2} \tag{5.5.4}$$

where m =0.494 GeV/c^2 and p the total momentum of the kaon candidate. Each value of the momentum components and the total energy of the K^+ and K^- candidates are added to obtain the momentum components and total energy of the potential ϕ meson. Then the invariant mass distribution of the ϕ meson can be calculated by Eq. 2.3.1 (in natural units)

$$m_{inv\phi} = \sqrt{E_\phi^2 - (p_{x\phi}^2 + p_{y\phi}^2 + p_{z\phi}^2)} \tag{5.5.5}$$

The background of the invariant mass distribution is obtained with the same procedure described above but with like-sign pairs instead, i.e. K^--K^- and K^+-K^+ pairs. If a signal of the ϕ meson is present, the invariant mass distribution of the unlike-sign pairs will show a peak around 1.02 GeV/c^2, which is the mass of the ϕ meson. A minimum and maximum cut, $1.017 < m_{inv} < 1.023$, is then made for the signal peak in order to isolate the events yielding number of ϕ meson candidates. The transverse momentum of each ϕ candidate is then obtained by Eq. 3.3.1 and its corresponding azimuthal angle φ by

$$\varphi = \frac{1}{2}\arctan\left(\frac{p_y}{p_x}\right) \tag{5.5.6}$$

To estimate the elliptic flow of the unlike-sign distribution, the azimuthal angle φ with respect to the event-plane Ψ_{EP} is represented as a function of p_T. The same representation is done for the like-sign distribution. The same procedure as explained in Sec. 5.4 is carried out to estimate the elliptic flow of the unlike-sign and like-sign particles but with a larger p_T binning, 0.6 GeV/c^2, due to less statistics.

The background for the extracted elliptic flow of ϕ is estimated by using the invariant mass distribution of unlike-sign particles, m_{invUS}, as a function of p_T and the invariant mass distribution of the like-sign particles, m_{invLS}, as a function of p_T. For each p_T bin of the m_{invUS}/m_{invLS} versus p_T histograms, an invariant mass distribution for a certain p_T interval is given by performing a projection on the y-axis. Then the obtained invariant mass distribution m_{invUS} for a p_T interval is integrated over the signal peak: $1.017 < m_{inv} < 1.023$. The m_{invLS}, in the same p_T interval as for m_{invUS}, is then integrated over the interval $1.03 < m_{inv} < 1.04$. Further, the obtained integral values for m_{invUS} and m_{invLS} are used for calculate the scale factor S. This is done by scaling the $m_{invUS}(1.017 - 1.023)$ integral value over the $m_{invLS}(1.03 - 1.04)$ integral value. Then the background ratio R can be obtained by using the scale factor S and integrating the m_{invLS} and the m_{invUS} over the signal peak

$$R = \frac{\int_{1.017}^{1.023} m_{invLS}(bin)}{\int_{1.017}^{1.023} m_{invUS}(bin)} S \tag{5.5.7}$$

The ratio R and the bin contents of the elliptic flow of like-sign v_{2LS} and unlike-sign particles v_{2US} are then used to estimate the elliptic flow of ϕ mesons $v_{2\phi}$ for each p_T bin. The elliptic flow v_2 is additive and this property can be used for estimate $v_{2\phi}$, the elliptic flow of ϕ mesons. First, the number of unlike-sign candidates N_{US} (in the signal peak interval) are assumed to be equal to the number of mesons N_ϕ and the background N_{BG}. Further by assuming that the background is approximately the number of like-sign candidate N_{LS}, the N_ϕ can be obtained

$$N_{US} = N_\phi + N_{BG} \approx N_\phi + N_{LS} \Rightarrow N_\phi \approx N_{US} - N_{LS} \tag{5.5.8}$$

The elliptic flow for unlike-sign candidates v_{2US} is then approximately

$$v_{2US} = \frac{(N_{US} - N_{LS})v_{2\phi} + N_{LS}v_{2LS}}{N_{US}} = (1 - R)v_{2\phi} + Rv_{2LS} \tag{5.5.9}$$

where $N_{LS}/N_{US} = R$ (R is given by Eq. 5.5.7). Hence, $v_{2\phi}$ is obtained by the following equation

$$v_{2\phi} = \frac{v_{2US} - Rv_{2LS}}{1 - R} \tag{5.5.10}$$

The invariant mass distribution of unlike-sign pairs and the corresponding scaled background of like-sign pairs in the p_T interval 2.4-3.0 GeV/c for the different centralities are presented in Fig. 5.5.

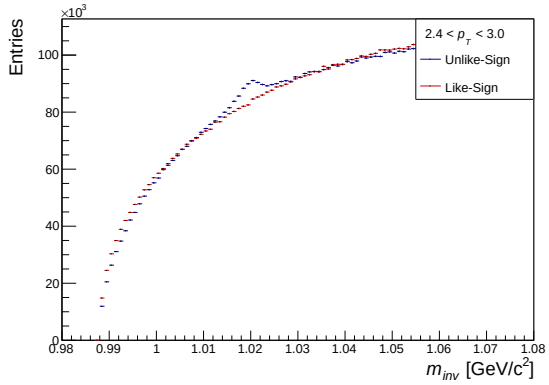

(a) 10-20% collision centrality

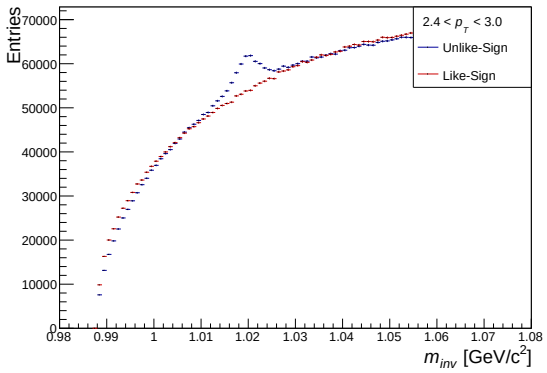

(b) 20-40% collision centrality

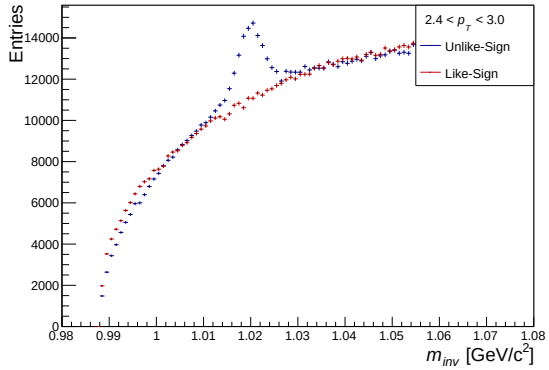

(c) 40-60% collision centrality

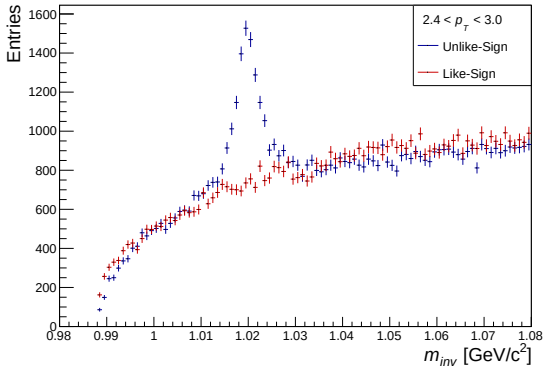

(d) 60-80% collision centrality

Figure 5.5: The invariant mass distribution for the ϕ meson and the estimated background in four different collision centralities in the range $2.4 < p_T < 3.0$.

5.6 Constituent-quark number scaling of the elliptic flow

To explore if the hadronic elliptic flow of all identified particles can be reduced to a universal elliptic flow of their constituent quarks, a scaling of v_2 is performed. For each particle species, the elliptic flow v_2 is divided by their respective valence quark number n_q. The scaled elliptic flow v_2/n_q for the identified particles is then represented as a function of the transverse kinetic energy divided by their respective valence quark number n_q

$$\frac{KE_T}{n_q} = \frac{m_T - m}{n_q} \tag{5.6.1}$$

where m_T is the transverse mass of the particle and m its mass. The scaled elliptic flow v_2/n_q is distributed over a $m_T - m$ interval up to 1.8 GeV/c^2 and presented as a graph.

5.7 Error analysis for the ϕ meson results

The statistical error analysis for each histogram used in this thesis is performed by the ROOT function *Sumw2*[31]. The function is defined as the sum of square of weights and gives the error propagation for each bin content of the histograms.

The error analysis for the elliptic flow of ϕ mesons is done by estimating the propagation of error[32]. The uncertainty σ of the extracted $v_{2\phi}$ (with f given by Eq. 5.5.10) is calculated by

$$\sigma_{v_{2\phi}} = \sqrt{\left(\frac{\delta f}{\delta US}\right)^2 \sigma_{US}^2 + \left(\frac{\delta f}{\delta LS}\right)^2 \sigma_{LS}^2 + \left(\frac{\delta f}{\delta R}\right)^2 \sigma_R^2} \tag{5.7.1}$$

where σ_{US} and σ_{LS} are the errors estimated by the weighted sum of squares for each p_T bin for the elliptic flow of unlike-sign and like-sign particles, respectively. The error for the ratio σ_R is calculated as follows

$$\sigma_R^2 = \left(\frac{1}{\int_{1.017}^{1.023} m_{invUS}(bin)} + \frac{1}{\int_{1.017}^{1.023} m_{invLS}(bin)}\right) R^2 \tag{5.7.2}$$

where R is given by Eq. 5.5.7. The partial derivatives are

$$\left(\frac{\delta f}{\delta US}\right)^2 = \left(\frac{1}{1-R}\right)^2, \qquad \left(\frac{\delta f}{\delta LS}\right)^2 = \left(-\frac{R}{1-R}\right)^2, \qquad \left(\frac{\delta f}{\delta R}\right)^2 = \left(\frac{v_{2US} - v_{2LS}}{(1-R)^2}\right)^2 \tag{5.7.3}$$

6 Results

This section presents the results of the elliptic flow v_2 as a function of p_T for all identified hadrons, as well as the scaling properties for pions, protons and kaons.

6.1 Elliptic flow $v_2(p_T)$

Figure 6.1.a, 6.1.b, 6.2.a and 6.2.b present the elliptic flow v_2 as a function of p_T of all identified particles for 10-20%, 20-40%, 40-60% and 60-80% collision centrality, respectively. The error bars for the ϕ meson correspond to the estimated uncertainty of the signal extraction described in Sec. 5.6. The error estimation, sum of square of weights, for the residual identified particles is also represented as error bars in the figures but significantly smaller than for the ϕ meson.

An increase of the v_2 value for all particle species in the p_T region $\sim$0.2-3.0 GeV/c can be observed from the most central collisions (i.e. 10-20%) used in this thesis up to the mid-central collisions, 20-40% and 40-60%. For the most peripheral collisions, 60-80%, a decrease of the v_2 for protons, pions and kaons in the whole p_T region occurs. In the same centrality (60-80%), a distinctive increase of the v_2 of the ϕ meson in the entire p_T regime is observed.

For the centrality intervals 10-20%, 20-40% and 40-60%, an approximately linear increase of the v_2 up to $p_T \lesssim 0.8$ GeV/c is exhibited for protons, pions and kaons. This increase of the v_2 for the three particle species is followed by a saturation at $p_T \gtrsim 2.5$ GeV/c. A crossing point occurs at $p_T \sim 2.0 - 2.5$ GeV/c for the three centrality intervals, where the v_2 of protons becomes higher than for pions and kaons. Before the crossing point occurs, $p_T \lesssim 2.0 - 2.5$ GeV/c, a clear mass ordering of the three particle species can be observed ($v_{2\pi} > v_{2K} > v_{2p}$). After the crossing point, a clear maximum of the v_2 can be observed for protons at $p_T \sim$3.0 GeV/c for 20-40% and 40-60% centrality. A maximum of v_2 for kaons and pions seems to occur at $p_T \sim$2.5-3.0 GeV/c in the centrality intervals 20-40% and 40-60%. These maxima are not as distinguishable as for protons.

The v_2 value trends of the ϕ meson are not as consistent as for protons, pions and kaons, but the ϕ error bars are significantly larger than for the other particle species. For $10 - 20\%$ centrality, the v_2 values of the ϕ meson in the entire p_T regime follow a similar pattern as for protons. In the mid-central collisions, 20-40%, an increase of the v_2 (compared to 10-20%) in the p_T region 1.2-2.4 GeV/c is shown. For 40-60%

centrality, an increase of the v_2 for ϕ compared to the more central intervals can be observed up to 3.0 GeV/c in p_T and may be followed by a decrease of the v_2.

6.2 Constituent-quark number scaling (CQNS)

Figure 6.3.a, 6.3.b, 6.4.a and 6.4.b present the $(m_T - m)/n_q$ dependence of the v_2/n_q for pions, protons, kaons and ϕ mesons in the centrality intervals 10-20%, 20-40%, 40-60% and 60-80%, respectively. As described in Sec. 5.6, $m_T - m/n_q$ is an estimate of the transverse kinetic energy EK_T divided by the number of quarks.

For all four centrality intervals, the value of v_2/n_q coincide for pions, protons and kaons up to $\sim$0.6 GeV/c^2. For $(m_T - m)/n_q \gtrsim 0.6$ GeV/c^2 in all centrality intervals, the pions and kaons continue to overlap over the remaining $(m_T - m)/n_q$ region. The protons are clearly separated from the pions and kaons for $(m_T - m)/n_q \gtrsim 0.6$ GeV/c^2 in the mid-central collisions (20-40% and 40-60%). This separation of protons is less significant for the most central and the most peripheral collisions (10-20% and 60-80%).

For pions and kaons, a saturation of the v_2/n_q seem to occur around $(m_T - m)/n_q$ $\sim$0.8-1.0 GeV/c^2 for all centrality intervals and this is sustained throughout the remaining $(m_T - m)/n_q$ region. For protons, the v_2/n_q starts to decrease after the separation from the pions and kaons at $(m_T - m)/n_q$ $\sim$0.6-0.8 GeV/c^2 for the mid-central collisions.

The ϕ meson can be observed to coincide, within the uncertainties, with the other identified particles up to $\sim$0.6 GeV/c^2 for the 10-20% and 20-40% centralities. For all centrality intervals except 60-80%, the ϕ meson tends (to a small degree) to follow the pattern of pions and kaons in the higher momentum regime, $(m_T - m)/n_q \gtrsim 0.8$ GeV/c^2. For the most peripheral collision centrality, the v_2/n_q values for the ϕ meson are very high above the other particle species, as expected from the results presented in Sec. 6.1.

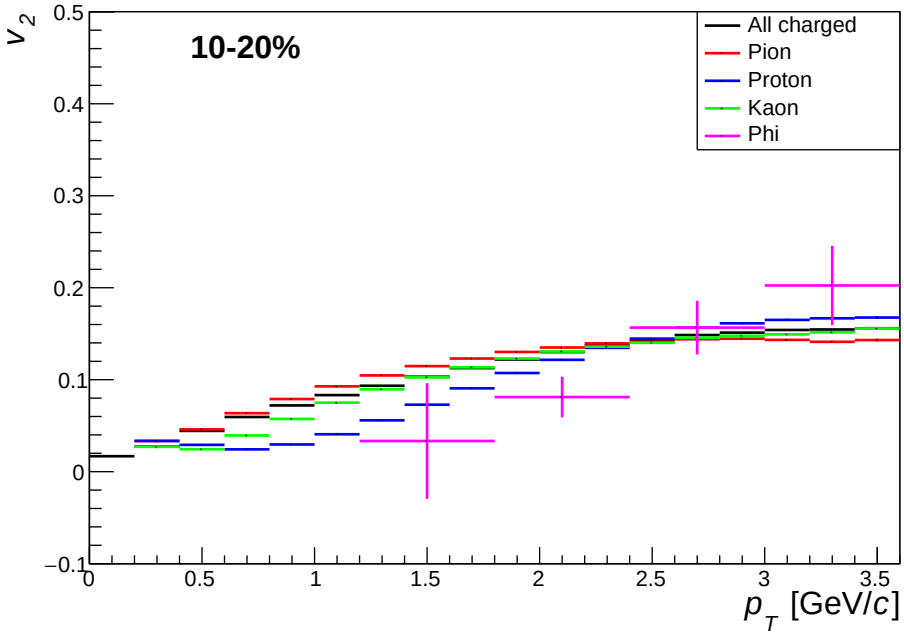

(a) 10-20% collision centrality

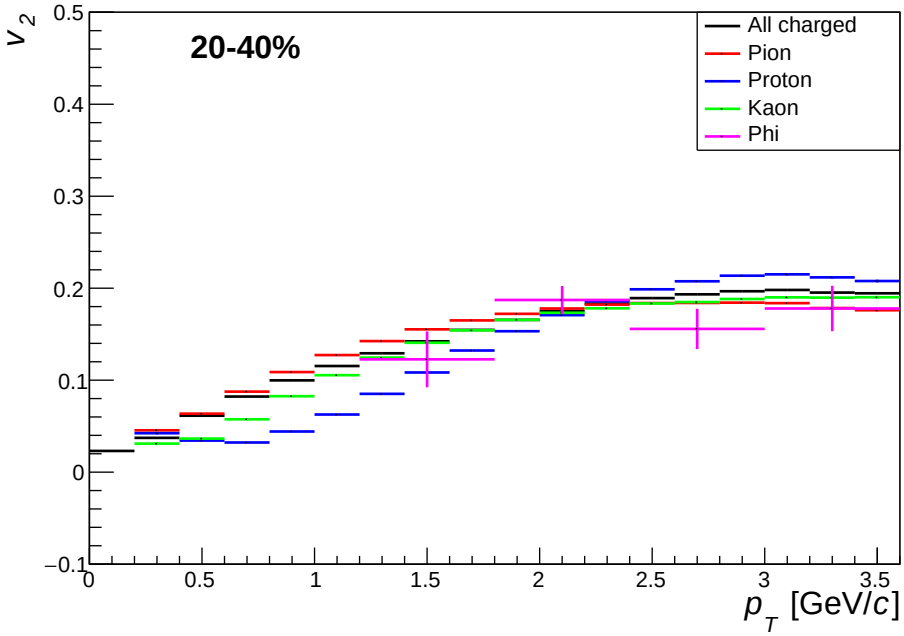

(b) 20-40% collision centrality

Figure 6.1: Extracted elliptic flow v_2 of all charged particles, pions, protons, kaons and ϕ mesons. The data originates from Pb-Pb collisions at $\sqrt{s_{NN}}$=2.76 TeV and 10-20% centrality for (a) and 20-40% centrality for (b).

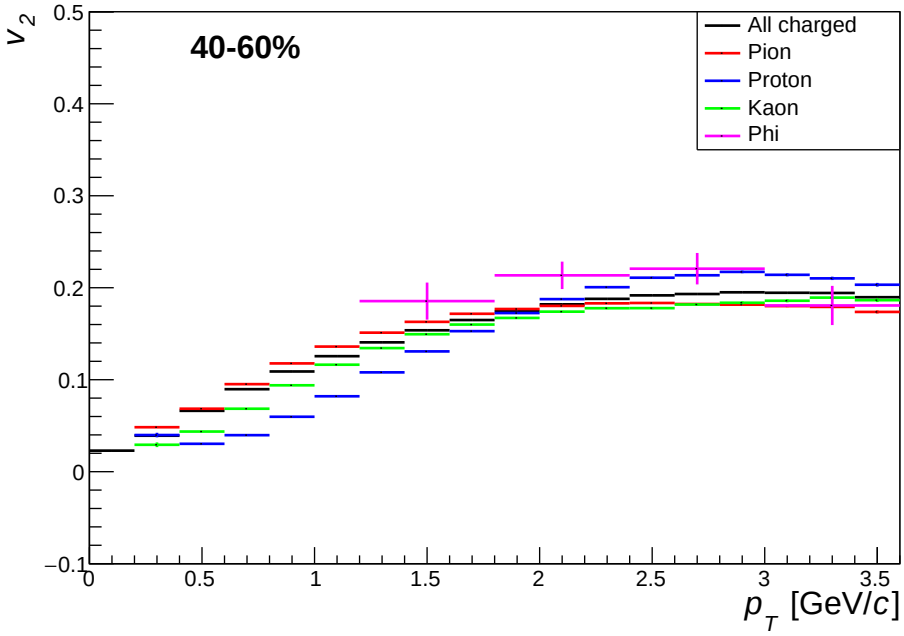

(a) 40-60% collision centrality

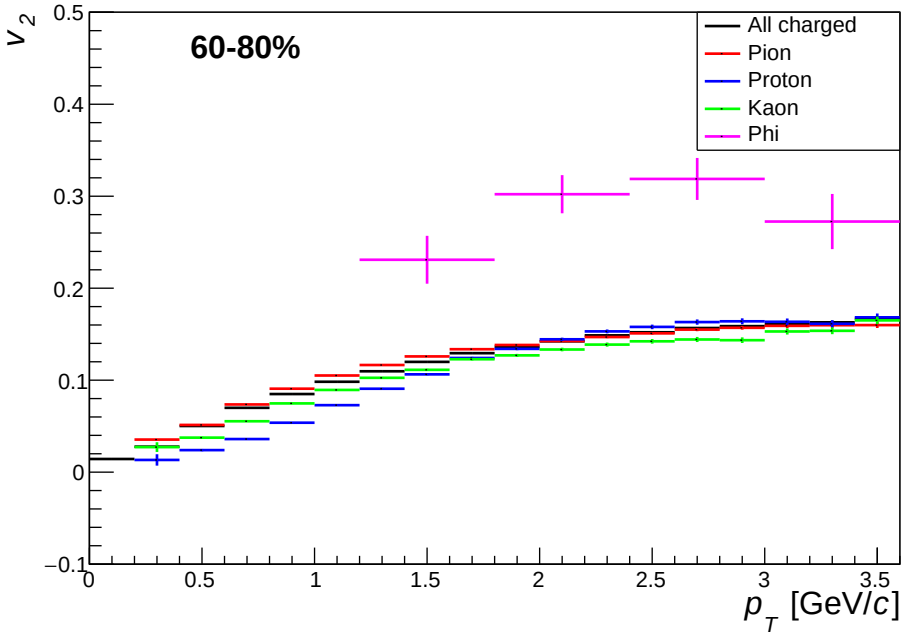

(b) 60-80% collision centrality

Figure 6.2: Extracted elliptic flow v_2 of all charged particles, pions, protons, kaons and ϕ mesons. The data originates from Pb-Pb collisions at $\sqrt{s_{NN}}$=2.76 TeV and 40-60% centrality for (a) and 60-80% centrality for (b).

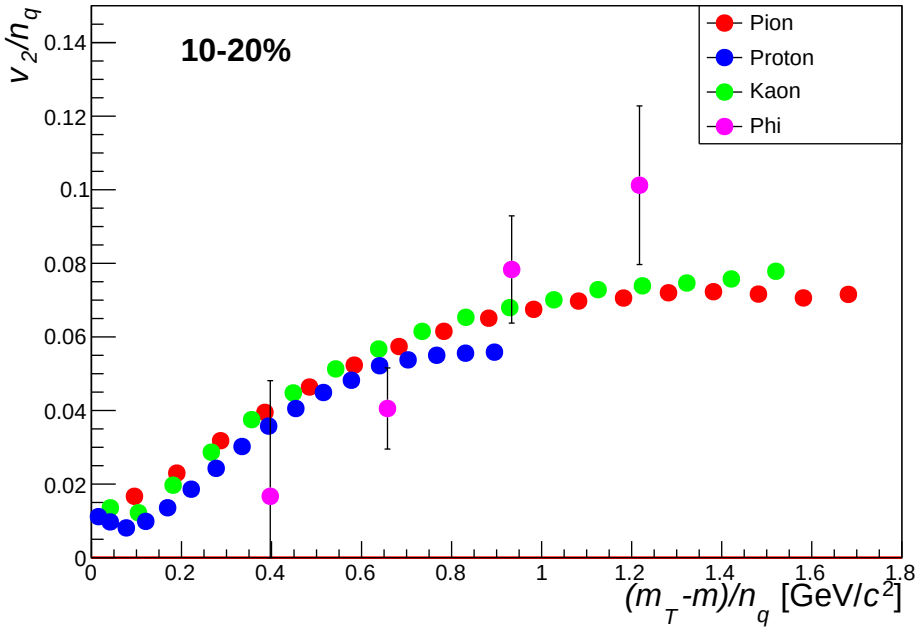

(a) 10-20% collision centrality

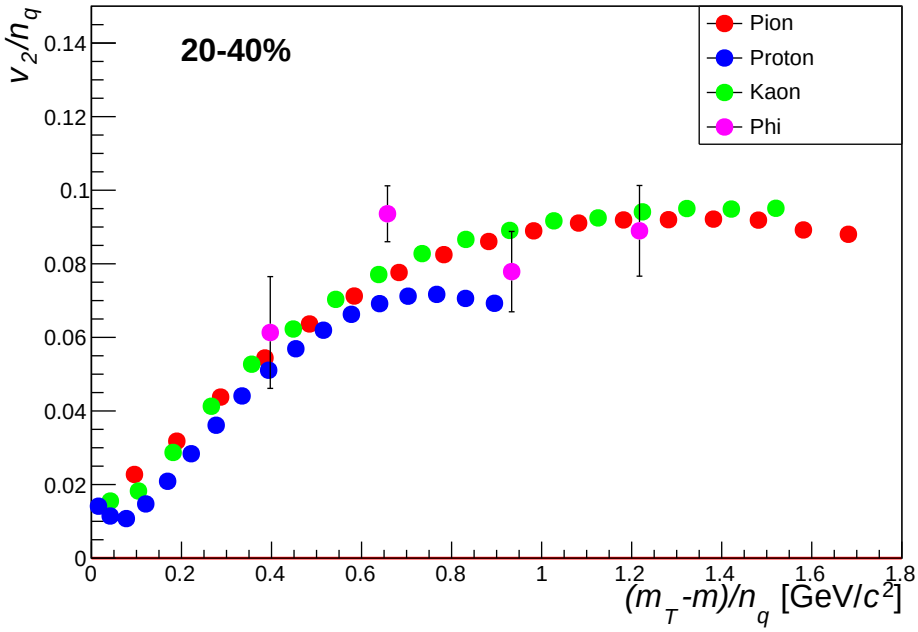

(b) 20-40% collision centrality

Figure 6.3: The $(m_T - m)/n_q$ dependence of v_2/n_q for pions, protons and kaons. The data originates from Pb-Pb collisions at $\sqrt{s_{NN}}$=2.76 TeV and 10-20% centrality for (a) and 20-40% centrality for (b).

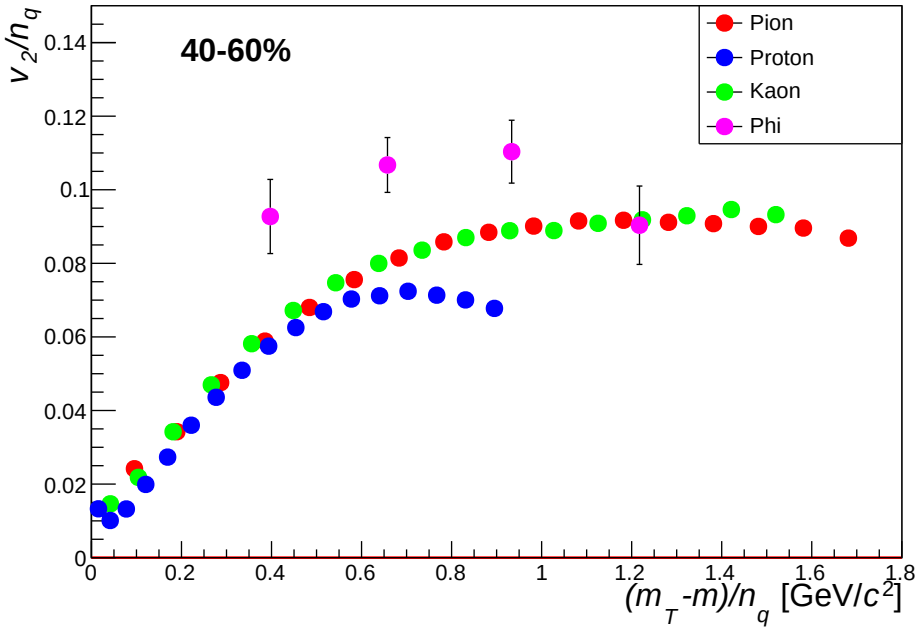

(a) 40-60% collision centrality

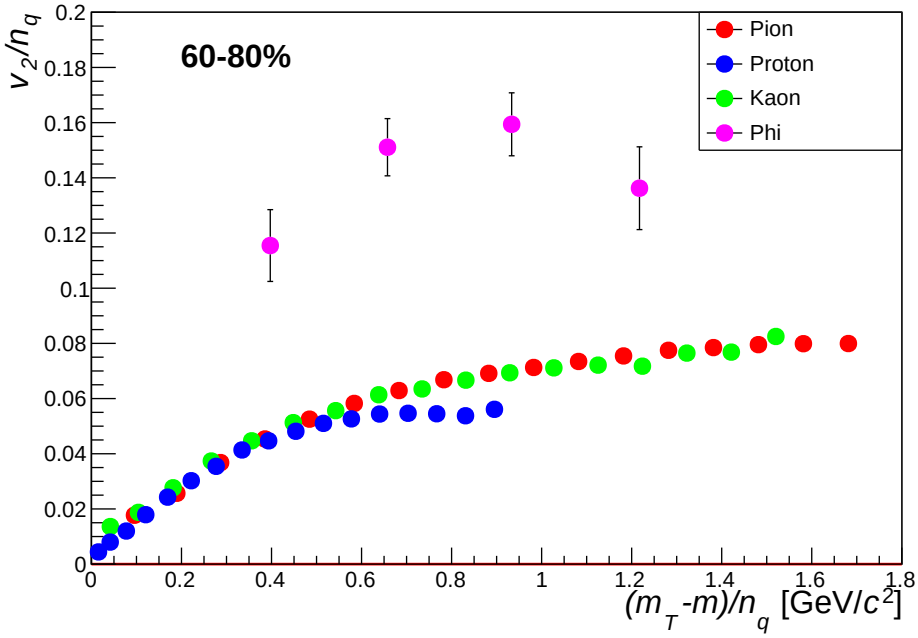

(b) 60-80% collision centrality

Figure 6.4: The $(m_T - m)/n_q$ dependence of v_2/n_q for pions, protons and kaons. The data originates from Pb-Pb collisions at $\sqrt{s_{NN}}$=2.76 TeV and 40-60% centrality for (a) and 60-80% centrality for (b).

7 Discussion

In this section the results from Sec. 6.1 and 6.2 will be discussed compared with the hydrodynamic model and the quark recombination model. The results of the $v_2(p_T)$ are discussed in the first part of the section and this is followed by a discussion of the constituent-quark scaling results.

7.1 Elliptic flow of the identified hadrons

The increase of the $v_2(p_T)$ values for protons, pions and kaons from central, 10-20%, to mid-central collisions, 40-60%, is consistent with the anisotropic expansion in momentum space depending on the geometry of the impact region at the collision point. In these centralities, a collision centrality dependent increase of the v_2 for the ϕ meson can also be observed for $p_T \lesssim 2.4$ GeV/c. In the very peripheral collisions (60-80%), the v_2 values for all identified particle species, except the ϕ, are reduced. This effect may arise from the large fluctuations and the smaller impact region in this collision centrality. According to [11], the reduction of the v_2 in very peripheral collisions could be due to an incomplete thermalization of the fireball, as it is much smaller and have a shorter life time. The ϕ meson in the 60-80% centrality shows an unexpected v_2 pattern and this may be due to reduced statistics and larger uncertainties at this centrality.

At all centralities, protons, pions and kaons in the lower p_T region, $\sim$0.6-2.0 GeV/c^2, exhibit a clear mass ordering, which is consistent with the hydrodynamic model. The ϕ meson also follows the mass ordering in the same p_T region, but only for 10-20% and 20-40% centralities. The mass ordering arises from the merged effects of radial and elliptic flow according to [33]. This suggests that the radial flow reduces the in-plane (more than the out-plane flow) by creating a depletion at low p_T values in the p_T spectrum that enhances with increasing mass of the particles. Hence, the v_2 is reduced for heavier particles. For $p_T \gtrsim 2.0$ GeV/c, the hydrodynamic model is insufficient as it predicts increasing v_2 with increasing p_T, and not the observed flattening trend.

For all centralities, a crossing point of protons, pions, and kaons occurs at p_T $\sim$2.0-2.8 GeV/c^2. At this point, the v_2 of protons obtains a higher value than for pions and kaons. This is expected by the quark recombination model, which predicts that the v_2 of baryons should be larger than the v_2 of mesons in the intermediate p_T range. In this range, p_T $\sim$2.0-3.0 GeV/c^2, the v_2 values are consistent with the quark recombination model as the pions and kaons can be observed to coincide, while the protons obtain higher v_2 values than these two particle species. However, the obtained v_2 results of the ϕ meson are ambiguous and do not show a clear coherence with this model.

7.2 Scaling properties

The assumption of the recombination model states that the quarks have an universal flow, which arises from the quark degrees of freedom being dominant during the hadronization stage. This effect on the v_2 can be observed to some degree in the results of the CQNS for protons, pions and kaons, presented in Sec. 6.2. At all centralities, the CQNS of the v_2 shows that the protons, pions and kaons approximately coincide for $m_T - m_0/n_q \lesssim 0.6$ GeV/c^2. For $m_T - m_0/n_q \gtrsim 0.6$ GeV/c^2, the protons are separated from the pions and kaons and thus the recombination model is no longer valid. This deviation from the recombination model can be due to other contributions at higher momentum such as jets.

The CQNS properties of the ϕ meson are difficult to interpret, which is expected due to the result presented in Sec. 6.1. In the low momentum regime for the 10-20% and 20-40%, the ϕ meson v_2 values overlap to some degree with the values for the other identified particles. However, the errors bars, as mentioned previously, are larger for the ϕ than for the other particles and hence it is harder to draw any firm conclusions.

8 Conclusions and Outlook

8.1 Conclusions

A certain conclusion whether the origin of the elliptic flow is dependent on the particles compositions and masses or on an universal quark flow will not be established by the results produced in this thesis. However, the collision centrality dependence of the v_2 results is consistent with the picture of the anisotropic expansion in momentum space being dependent on the impact parameter b, i.e. the geometrical shape of the impact region and the number of participants at the collision point.

A distinct mass ordering of protons, kaons and pions for $p_T \sim$ 0.2-2.0 GeV/c could be observed at all centralities and this is in good agreement with the hydrodynamic model.

The results of scaling by the constituent-quark number of v_2 as a function of the scaled transverse kinetic energy KE_T are consistent with the recombination model in the lower momentum region. This can be interpreted as the quark coalescence effects survive into the hadronization stage.

Publications from the ALICE experiment do not take the 60-80% centrality interval into account due to the large fluctuations at this centrality and hence no clear elliptic flow can be observed. In this thesis the result from this centrality (60-80%), in Fig.6.2.b, demonstrates the difficulties to distinguish a clear elliptic flow signal for all particle species identified.

8.2 Outlook

In order to improve the results presented in this thesis a more quantitative PID of protons, pions and kaons is essential. A cleaner and more careful separation of the particle species to avoid false candidates and background could have been performed given more time. By using information from both the TOF β distribution as a function of p and the TPC dE/dx distribution as a function of p_T, a comparison between the PIDs for each particle species could have been carried out and this would also have provided a more precise PID of the particle species.

The azimuthal momentum distribution could have been improved by a more advanced event-plane analysis. This could have been achieved by including weight and resolution factors in the calculation of the event-plane.

To reduce the statistical fluctuation and improve the PID of the ϕ meson a larger amount of events, and thus tracks, would have been beneficial. More tracks would have enhance the number of identified K^+ and K^- candidates and hence the estimation of the elliptic flow for the ϕ meson could have been improved.

The background estimation for the ϕ meson could also been improved by a mixed-event study, in which the tracks of an event is combined with tracks from different events. By performing a mixed-event study the statistical uncertainty of the background could have been reduced.

To compare the CQNS properties of baryons and mesons in the higher momentum regime, the analysis for the $v_2(p_T)$ had to be carried out for a larger p_T interval than for this thesis (that is up to $p_T = 3.6$ GeV/c). For reliable values in the high p_T region more data is required due to less tracks produced for high p_T.

Finally, to fully evaluate the results for the ϕ meson analysis and the 60-80% centrality bin results, systematic uncertainties would need to be estimated.

Acknowledgements

First of all I would like to give many thanks to my supervisor David Silvermyr. His support and feedback during the whole project has been invaluable. I would like to thank Peter Christiansen for all the help regarding the programming, and also for his feedback on this thesis. Furthermore, I thank Tuva Richert, Martin Ljunggren and Vytautas Vislavičius for sharing their knowledge on particle physics and programming. I would also like to thank Adrian Nassirpour for the help and support during the project. Finally, many thanks to Evert Stenlund and Anders Oskarsson for sharing their expertise in the field and for their feedback on this thesis.

References

[1] Quantum Day. *Light Pulses From Quark Gluon Plasma To Accurately Measure Time in Septillionths of a Second*. @http://www.quantumday.com/2012/11/light-pulses-from-quark-gluon-plasma-to.html;. [2015-12-10].

[2] CERN. *Heavy ions and quark-gluon plasma*. @http://home.cern/about/physics/heavy-ions-and-quark-gluon-plasma;. [2015-12-06]

[3] A. K. Chaudhuri, *A short course on Relativistic Heavy Ion Collisions*, arXiv:1207.7028 [nucl-th]. (2012).

[4] M. He, R. J. Fries and R. Rapp, *Scaling of Elliptic Flow, Recombination and Sequential Freeze-Out of Hadrons in Heavy-Ion Collisions*, Phys. Rev. C **82**, 034907 (2010) doi:10.1103/PhysRevC.82.034907 [arXiv:1006.1111 [nucl-th]].

[5] A. Datta A, B. Muhkopadhyaya, A. Raychaudhuri. *Physics at the Large Hadron Collider*. New Delhi; 2009.

[6] B. R. Martin, G. Shaw. *Particle Physics*. 3rd ed. John Wiley & Sons; 1993.

[7] W. Florowski. *Phenomenology of Ultra-Relativistic Heavy-Ion Collisions*. World Scientific Publishing; 2010.

[8] Universität Zürich, Physik-institut. *Standard Model*.
@http://www.physik.uzh.ch/groups/serra/StandardModel.html;. [2015-12-06].

[9] K.A. Olive et al. (Particle Data Group). *REVIEW OF PARTICLE PHYSICS*. Chinese Physics C 38, 090001 (2014).

[10] P. Braun-Munzinger, J. Stachel. *The quest for the quark–gluon plasma*. Nature 448, 302-309 (2007).

[11] R. C. Hwa, XN. Wang. *Quark-Gluon Plasma 3*. World Scientific Publishing; 2004.

[12] R. J. Fries, *Quark Recombination in Heavy Ion Collisions*, PoS CERP **2010**, 008 (2010) [arXiv:1102.5723 [nucl-th]].

[13] S. K. Prasad, S. Das, S. K. Ghosh, P. Ghosh, S. Muhuri, T. K. Nayak and R. Ray, *"Soft" and "hard" interactions in proton-proton collisions at LHC energies*, Proc. Indian Natl. Sci. Acad. **81**, no. 1, 213 (2015). doi:10.16943/ptinsa/2015/v81i1/48071.

[14] J. M. Campbell, J. W. Huston and W. J. Stirling, *Hard Interactions of Quarks and Gluons: A Primer for LHC Physics*, Rept. Prog. Phys. **70**, 89 (2007) doi:10.1088/0034-4885/70/1/R02 [hep-ph/0611148].

[15] R. Snellings, *Collective Expansion at the LHC: selected ALICE anisotropic flow measurements*, J. Phys. G **41**, no. 12, 124007 (2014) doi:10.1088/0954-3899/41/12/124007 [arXiv:1408.2532 [nucl-ex]].

[16] X. Wei. *PHENIX Reaction Plane Detector*. @https://www.bnl.gov/rhic/news/061907/story2.asp;. [2016-12-03].

[17] B. Muller, J. Schukraft and B. Wyslouch, *First Results from Pb+Pb collisions at the LHC*, Ann. Rev. Nucl. Part. Sci. **62**, 361 (2012) doi:10.1146/annurev-nucl-102711-094910 [arXiv:1202.3233 [hep-ex]].

[18] C. R. Hwa, XN. Wang. *Quark-gluon Plasma 4*. World Scientific Publishing; 2010.

[19] B. B. Abelev *et al.* [ALICE Collaboration], *Performance of the ALICE Experiment at the CERN LHC*, Int. J. Mod. Phys. A **29**, 1430044 (2014) doi:10.1142/S0217751X14300440 [arXiv:1402.4476 [nucl-ex]].

[20] E. Abbas *et al.* [ALICE Collaboration], *Performance of the ALICE VZERO system*, JINST **8**, P10016 (2013) doi:10.1088/1748-0221/8/10/P10016 [arXiv:1306.3130 [nucl-ex]].

[21] CERN. *The Large Hadron Collider*. @http://home.cern/topics/large-hadron-collider;. [2015-12-01].

[22] CERN press office. *CERN's Large Hadron Collider gears up for run 2*. @http://press.web.cern.ch/press-releases/2014/12/cerns-large-hadron-collider-gears-run-2;. [2015-12-01].

[23] The ALICE experiment. *Inside Alice. Overview of a particle detector*. @http://aliceinfo.cern.ch/Public/en/Chapter2/Chap2InsideAlice-en.html;. [2015-12-03].

[24] CERN; ALICE. *ALICE detects quark-gluon plasma, a state of matter thought to have formed just after the big bang*. @http://home.cern/about/experiments/alice;. [2015-12-02].

[25] The ALICE experiment. *The ALICE Time Projection Chamber (TPC)*. @http://aliceinfo.cern.ch/Public/en/Chapter2/Chap2_TPC.html;. [2015-12-02].

[26] J. Alme *et al.*, *The ALICE TPC, a large 3-dimensional tracking device with fast readout for ultra-high multiplicity events*, Nucl. Instrum. Meth. A **622**, 316 (2010) doi:10.1016/j.nima.2010.04.042 [arXiv:1001.1950 [physics.ins-det]].

[27] D. T. Larsen. *Monitoring and calibration of the ALICE time projection chamber*. PhD dissertation. University of Bergen. June 2010.

[28] The ALICE experiment. *The ALICE Time of Flight Detector*.
@http://aliceinfo.cern.ch/Public/en/Chapter2/Chap2_TOF.html;. [2015-12-02].

[29] ROOT. *Data Analysis Framework*. @https://root.cern.ch/drupal/;. [2015-11-29].

[30] A. Bilandzic, N. van der Kolk, J. Y. Ollitrault and R. Snellings, *Event-plane flow analysis without non-flow effects*, Phys. Rev. C **83**, 014909 (2011) doi:10.1103/PhysRevC.83.014909 [arXiv:0801.3915 [nucl-ex]].

[31] ROOT. *TH1 Class Reference*. @https://root.cern.ch/doc/master/classTH1.html;. [2015-12-06].

[32] R. W. Leo. *Techniques for Nuclear and Particle Physics Experiments, A How-to Approach*. 1st ed. Springer-Verlag; 1987.

[33] B. B. Abelev *et al.* [ALICE Collaboration], *Elliptic flow of identified hadrons in Pb-Pb collisions at* $\sqrt{s_{\rm NN}} = 2.76$ *TeV*, JHEP **1506**, 190 (2015) doi:10.1007/JHEP06(2015)190 [arXiv:1405.4632 [nucl-ex]].